Energy & Environmental Science

Maximizing power generation from ambient stray magnetic fields around smart infrastructures enabling self-powered wireless devices

Journal:	*Energy & Environmental Science*
Manuscript ID	EE-ART-12-2019-003902.R1
Article Type:	Paper
Date Submitted by the Author:	12-Jan-2020
Complete List of Authors:	Lee, Hyeon; Virginia Polytechnic Institute and State University Sriramdas, Rammohan; Virginia Polytechnic Institute and State University Kumar, Prashant; Virginia Polytechnic Institute and State University, Mechanical engineering Sanghadasa, Mohan; U.S. Army, Aviation and Missile Research, Development, and Engineering Center, Weapons Development and Integration Directorate Kang, Min-Gyu; Pennsylvania State University, Department of Materials Science and Engineering; Virginia Polytechnic Institute and State University, Center for Energy Harvesting Materials and Systems Priya, Shashank; Virginia Polytechnic Institute and State University, Center for Energy Harvesting Materials and System; Virginia Polytechnic Institute and State University, Department of Mechanical Engineering; Pennsylvania State University, Department of Materials Science and Engineering

Energy & Environmental Science

ARTICLE

Maximizing power generation from ambient stray magnetic fields around smart infrastructures enabling self-powered wireless devices

Received 00th January 20xx,
Accepted 00th January 20xx

DOI: 10.1039/x0xx00000x

www.rsc.org/

Hyeon Lee,[a] Rammohan Sriramdas,[a,c] Prashant Kumar,[a] Mohan Sanghadasa,[b] Min Gyu Kang,*[a,c] and Shashank Priya*[a,c]

Harvesting electrical energy from stray magnetic fields is appealing for development of a sustainable power source for Internet of Things (IoT) devices that are being implemented in the smart infrastructure. The stray magnetic fields are ubiquitous in the buildings, but have low fixed frequency (50/60 Hz) and low amplitude. Magnetoelectric (ME) coupled magneto-mechano-electric (MME) energy conversion is the most efficient way to convert these low frequency stray magnetic fields into electricity. However, currently reported ME coupled MME generators produce high output power only under relatively strong magnetic field (≥ 500 μT), which are not available in practical conditions. Here the novel ME coupled MME generator is demonstrated that provides 400% higher output power compared to the state-of-the-art, when operating below magnetic field levels of 100 μT. The optimized ME coupled MME generator produces milliwatt power below 300 μT stray magnetic field. The output power from extremely low magnetic fields (≤ 50 μT) is sufficient to power hundreds of light emitting diode (LED) arrays and operate a digital clock without charging a capacitor. By exploiting the harvested power near a home appliance, sustainable powering of sensors and a wireless communication system is demonstrated. Fundamental advancements from this work will provide direction for deploying ME and MME generator driven self-powered IoT devices in the smart infrastructures.

Broader context

Low-magnitude magnetic field exist in our surroundings as a by-product of electric current flow. Traditionally, the stray magnetic field has been considered as a noise and thus it has been avoided. Results in this study show that it can be a useful ubiquitous energy source. Magnetic fields from industrial and residential infrastructures, such as domestic appliances, lights, power cables, etc., are strong enough to provide power for variety of electronics. A promising method is demonstrated to scavenge this wasted magnetic field energy and convert it into usable electricity. This method has potential to provide a sustainable power source for the Internet of Things (IoT) sensors and wireless communication systems deployed in smart homes and smart factories. Commercially available radio frequency (RF) antenna and induction coils convert the RF magnetic fields into electric power. However, their energy conversion efficiency tends to be dramatically degraded at low frequencies (50/60 Hz). Here, strategies for designing low-frequency energy conversion devices are provided to achieve high power density at low frequency and under low amplitude magnetic fields. Magnetoelectric (ME) coupled magneto-mechano-electric (MME) energy conversion mechanism can provide high output power under ambient conditions and is easy to integrate onto various smart infrastructures. Comprehensive modelling and experiments are conducted to analyse the variation of output voltage and power under practical conditions. ME coupled MME generators comprising of piezoelectric and magnetostrictive materials are shown to provide the highest output power in the low frequency range (≤ 300 μT) among currently reported MME generators. These results provide significant advancements towards sustainable power based integrated sensors and wireless communication systems.

1. Introduction

Smart infrastructure based upon the Internet of Things (IoT) will comprise of interconnected devices such as home appliances, transportation, and smart manufacturing. Wireless sensor networks are critical components facilitating the implementation of the IoT. For example, the interconnected sensors monitor energy consumption and operational patterns of the utilities, assisting in

[a] Center for Energy Harvesting and Systems (CHEMS), Virginia Tech, Blacksburg, VA 24061, USA. Email: mgkang@psu.edu, sup103@psu.edu
[b] Aviation and Missile Center, U.S. Army Combat Capabilities Development Command, Redstone Arsenal, AL 35898
[c] Department of Materials Science and Engineering, Pennsylvania State University, University Park, PA 16802, USA

Electronic Supplementary Information (ESI) available: Material parameters for the modelling, Summary of modelling results, The attributes and simulation results for the ME coupled MME generators, Magnetostriction curve of pristine amorphous FBS alloy sheet, Geometries of the three different ME coupled MME generators and fabrication method, Experimental setup for magnetic energy harvesting, Acceleration measurement setup, Output voltages of the ME coupled MME generators under various applied AC magnetic field, Modelling condition for stress and piezoelectric potential analysis, Frequency dependent dielectric properties of a single piezoelectric sheet, Displacement, strain, stress, and piezoelectric potential profiles in MME generators under various applied magnetic fields, Measured and modelled output voltages as function of load resistance and applied AC magnetic field, Impedance of the M4 generator as function of frequency, Average power of the ME coupled MME generators, Powering LED arrays, Electric circuit design for charging capacitors, Movie S1: Powering LED arrays under various AC magnetic field strength, Movie S2: Powering a small incandescent light bulb using charged power in 1 F supercapacitor, Movie S3: Powering 180 LED arrays at 10 cm away from the space heater, Movie S4: Powering a digital clock at 20 cm away from the space heater, Movie S5: Powering an integrated sensor and wireless communication system at 4.5 cm away from the space heater. See DOI: 10.1039/x0xx00000x

remote control of objects within buildings and manufacturing plants, and providing a direct interface between a user and their environment. The IoT allows the efficient energy management of infrastructure, and enhances the quality of services for customers and residents with lower cost.[1-4] However, the implementation of wireless sensor networks at large scale is challenging, as these sensors require availability of consistent power source. Although microelectronics with extremely low power consumption have been developed for IoT application,[5] powering wireless sensor system using only batteries or capacitors is not a practical solution because of their limited life time.[6] Wiring hundreds of the IoT sensors to grid power supply is also not a practical solution as it increases the complexity of integration and cost within the current infrastructures. Ideally the IoT devices in smart infrastructures need to be powered by sustainable and wireless power sources from their ambient environment.

Energy harvesting technology allows generation of electrical power from surrounding wasted energy sources such as vibration,[7-12] heat,[13-15] light,[16, 17] ocean waves,[18, 19] and stray magnetic fields.[20-27] Among them, the stray magnetic field, which is generated around electric current flow, is a promising energy source as it exists everywhere within modern infrastructure, e.g. home appliances, lights, and electronic devices. To convert the magnetic field into electricity, various energy conversion mechanisms have been investigated. The most common mechanism is Faraday's law of induction, which has been utilized for wireless power transfer such as magnetic resonance [28, 29] and rectenna in radio frequency regime[30]. However, stray magnetic fields around infrastructure have fixed low frequency (50 or 60 Hz). Therefore, a novel energy conversion mechanism is required for high energy conversion efficiency and power density in the low frequency range.

Magneto-mechano-electric (MME) energy conversion mechanism has been shown to generate high power density from low frequency magnetic fields. The MME generator includes two steps to convert AC magnetic field into electric field. First, the magnetic field is converted into mechanical vibration through excitation of the permanent magnet. Next, the electric field is generated from the mechanical vibration through direct piezoelectric effect. The MME generator comprises of a piezoelectric cantilever structure with a permanent magnetic tip mass, and is designed to resonate in the fundamental mode at low frequency.[24, 27]

Recently, strain-mediated magnetoelectric (ME) effect, which is a coupling between magnetostriction and piezoelectricity, has been employed to enhance the performance of MME generators, termed as ME coupled MME generators. The ME coupled MME generator has a similar structure as that of the MME generator, but the elastic body is replaced by the magnetostrictive material that generates strain under magnetic field. The magnetostriction of the elastic body plays an important role in amplifying the bending moment of the MME cantilever under alternative magnetic fields.[21, 23] Performance of the ME coupled MME generator is determined by the mechanical coupling coefficients of both magnetostrictive (piezomagnetic coefficient) and piezoelectric materials (piezoelectric coefficient).

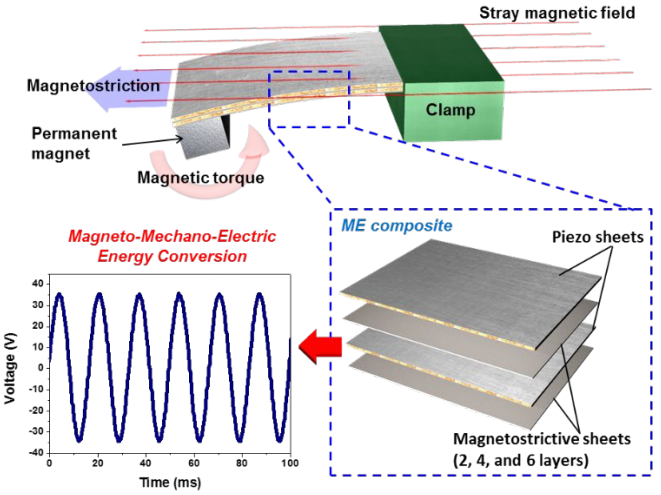

Fig. 1 Schematic description of working mechanism of the ME coupled MME generator and structural design to generate high electrical power under low magnetic field.

Magnetostrictive materials that have high piezomagnetic coefficient at low magnetic field such as nickel,[20, 22, 26] amorphous $Fe_{85}B_5Si_{10}$ (FBS) alloy,[21] and Fe-Ga alloy,[23] exhibit high ME coupling as well as provide high output power from the MME generators when combined with the single-crystalline macro fiber composite (SMFC),[20, 22, 23, 26] or piezoelectric macro fiber composite (MFC).[21] An ME coupled MME generator comprising of a textured Fe-Ga alloy and $[Pb(Mg_{1/3}Nb_{2/3})O_3\text{-}Pb(Zr,Ti)O_3]$ (PMN-PZT) SMFC has been shown to produce milliwatt power under 700 μT magnetic field at 60 Hz.[23] Most of the reported MME generators have been designed to operate under strong magnetic fields higher than 500 μT.[20, 22, 23] However, according to the International Commission on Non-Ionizing Radiation Protection (ICNIRP), the reference limit levels for general public and occupational exposures of 60 Hz magnetic field to human body are ~80 μT and ~420 μT, respectively.[31] Furthermore, the guideline limit for general public exposure of magnetic field level recommended from World Health Organization (WHO) is 100 μT, and the magnetic field strength at a distance of 30 cm from most household appliances is mostly below the guideline limit.[32] Therefore in practice, the stray magnetic field level from the common infrastructural devices is much lower than the operation range of previously reported MME generators. It is imperative that new designs for MME generator are required that produce higher electrical power under low magnetic field level in order to achieve sustainable powering of the IoT devices.

Here, we provide a new direction for the ME coupled MME generator to achieve high energy conversion efficiency under low amplitude magnetic fields (≤300 μT). The energy conversion steps in the ME coupled MME generator and influence of structural components determining the energy conversion efficiency and power density are investigated through the combination of theoretical and experimental approaches. It is shown that mutually coupled mechanical parameters, such as flexural rigidity, volume of the magnet, and geometrical factors, have significant effects on both ME and MME energy conversion. Based upon the mechanism study,

an outstanding ME coupled MME generator is demonstrated that can generate milliwatt level power at applied magnetic field levels below 300 μT. The ME coupled MME generator exhibited ~400% increase in output power compared to previously reported generators in the low magnetic field range. Hundreds of LEDs and micro devices were powered by directly connecting them to the generator operating under an extremely low magnetic field of 50 μT. Furthermore, the performance of the developed ME coupled MME generator using polycrystalline materials is comparable with that of state-of-the-art ME coupled MME generators utilizing extremely expensive single-crystalline piezoelectric composite and textured magnetostrictive alloys under high magnetic fields. Using the output power from the ME coupled MME generator near home appliances, sustainable powering of integrated sensor and wireless communication systems is demonstrated.

Results and Discussion

ME coupled MME generator design for low amplitude magnetic field energy harvesting

To achieve efficient power generation from low amplitude magnetic fields, a novel ME coupled MME generator was designed as illustrated in Fig. 1. The generator is comprised of two piezoelectric ceramic plates and two magnetostrictive metal laminates. The layers were alternatively laminated using an epoxy adhesive and electrically connected in series across the layers. A standard PZT-5A type soft piezoelectric ceramics, which possess high electromechanical coupling coefficients (d_{31}=-190 pC/N), and amorphous FBS alloys known as Metglas (2605SA), possessing high saturation magnetostriction (27 ppm) at low magnetic fields below 2 mT (Fig. S1), were used as the active materials to maximize ME coupling. Permanent magnet tip mass was attached at the beam-end, which plays three roles: (i) generating magnetic torque driving magneto-mechanical vibration under AC magnetic fields, (ii) matching the resonance frequency of the MME generator to source frequency of 60 Hz, and (iii) applying DC magnetic field across the beam for promoting ME coupling. The other end of the beam was rigidly clamped to produce fundamental bending vibration under external magnetic field. The overall structure of the generator is comparable to the bimorph piezoelectric cantilever but was asymmetrically designed to produce bending moment through the magnetostriction of the Metglas layers, which amplifies the magneto-mechanical vibration. The details of the sample configuration and measurement system setup are provided in the supporting information S2 (Fig. S2 and S3).

Previously, we have discovered that ME coupled bending moment amplifies the magnitude of the overall magneto-mechanical vibration in the MME generators. Optimum flexural rigidity of the overall structure of the MME generator is an important factor for maximizing degree of stress transfer into the piezoelectric layers from magneto-mechanical vibration, resulting in dramatically enhanced power generation from the stray magnetic field.[21] Building upon prior results, we have designed the MME generator to achieve (i) high ME bending moment, (ii) high magnetic torque from the tip mass, and (iii) high stress magnitude in the piezoelectric layers at extremely low AC magnetic field. Since the resonance frequency is fixed at 60 Hz, the flexural rigidity of the MME generator is strongly correlated with the ME bending moment and magnetic torque. For the bending vibration, the resonance frequency of the cantilever beam can be defined as,[33, 34]

$$\omega_0 = \sqrt{\frac{k_{eq}}{m_{eq}}} = \sqrt{\frac{3EI/L^3}{(33/140)mL + M_t}} \quad (1)$$

where, k_{eq}, m_{eq}, EI, L, m, and M_t are the equivalent spring rate, equivalent mass, flexural rigidity of the beam, length of the beam, mass per unit length, and tip mass, respectively. This relation indicates that the flexural rigidity, length of the beam, and weight of the tip mass are complementary factors to fix the resonance frequency. The magneto-mechanical vibration is generated by the magnetic tip mass when the magnetic polarization is perpendicularly aligned with the external AC magnetic field. The magneto-mechanical torque (τ) of the permanent magnet under external magnetic field (B) can be expressed as:[35]

$$\boldsymbol{\tau} = (\boldsymbol{M} \times \boldsymbol{B}) \cdot \boldsymbol{V} \quad (2)$$

where, M and V are magnetization and volume of the permanent magnet, respectively. From Eqs. (1) and (2), it can be concluded that the total volume (or weight) of the permanent magnet determines the resonance frequency and amplitude of the magneto-mechanical vibration of the MME generator. Thus, incorporation of heavy magnetic tip mass and larger volume of the magnetostrictive materials will result in generation of high magnetic torque and ME bending moment, respectively. This will directly correlate with enhanced power output under low magnetic fields. Because the resonance frequency is fixed at 60 Hz, we have modified the MME generator structure with a low aspect ratio (31 mm (W) × 36 mm (L)) to incorporate the heavy permanent magnetic mass.

Next, to maximize magneto-mechanical vibration under low magnetic fields, we have modulated the flexural rigidity of the generator by varying total number of the laminated magnetostrictive sheets as 2, 4, and 6 layers. Henceforth, these harvesters will be referred as 2M, 4M, and 6M, respectively. The high flexural rigidity increases resonance frequency of the MME generator, which enables the inclusion of heavier magnetic mass. The large volume of the magnetostrictive phase in the MME generator enhances the ME bending moment under AC magnetic fields. Following this analysis, we have studied the influence of the flexural rigidity on the ME coupled bending moment and magneto-mechanical stress on the piezoelectric layers under low AC magnetic fields below 300 μT.

Relationship between flexural rigidity, stress, and performance of the MME generator

The ME coupled MME generator design requires a balance between the flexural rigidity and ME coupled magneto-mechanical vibration to maximize induced internal stress and piezoelectric potential. To match the resonance frequency of the MME generators to 60 Hz, permanent magnets were attached on the M2, M4, and M6 generator with weights of 11 g, 18.9 g, and 24.6 g, respectively. The tip mass acceleration amplitude and output peak voltage were obtained at the resonance frequency under various external AC

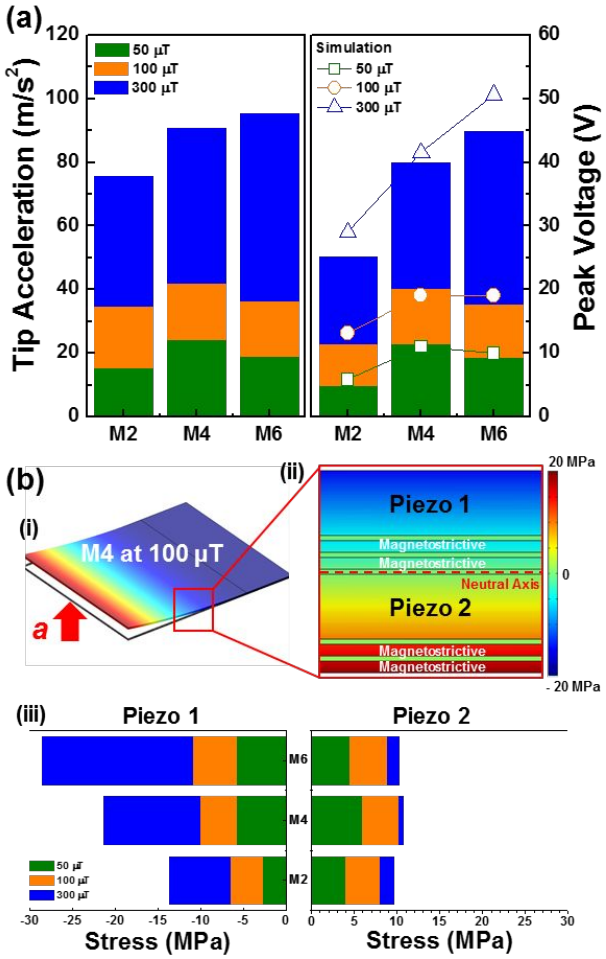

Fig. 2 Relationship between stress and piezoelectric potential in MME generator. (a) Tip acceleration (left) and generated piezoelectric potential (right) of the MME generators under various AC magnetic fields. Bar graphs and line graphs with symbols present experimental and simulation results, respectively. The piezoelectric potential is an open circuit voltage from the MME generators. (b) Modelling of internal stress profile in the MME generator (i) Displacement profile in M4 generator under 100 μT magnetic field and corresponding (ii) Internal stress profile. (iii) Internal stress in each piezoelectric layer of the MME generators. The stress values were collected at the center of each piezoelectric layer.

magnetic fields of 50, 100, and 300 μT (Fig. 2a). Details of the experimental method for measuring the tip acceleration are provided in supporting information (Fig. S4). The tip acceleration reflects the total magneto-mechanical vibration amplitude, which is the sum of the magnetic torque from the magnetic tip mass, and ME bending moment from the magnetostrictive layers. The tip acceleration is found to increase with increasing magnetic field strength and weight of the magnetic tip mass, but it shows different behavior below 100 μT. Although the M6 generator possesses heavier magnetic mass, its tip acceleration amplitude is found to be lower than M4 generator below 100 μT. Generally, tip deflection at the free end (δ_{tip}) of the cantilever is defined in terms of the flexural rigidity (*EI*), bending moment at the free end (*M*), and length of the cantilever (*L*);[36, 37]

$$\delta_{tip} = \frac{ML^2}{2EI} \quad (3)$$

This relationship indicates that the cantilever having higher flexural rigidity requires higher bending moment to generate the same level of deflection. In case of M6 generator, heavier magnetic mass and larger volume of the magnetostrictive sheets produces higher net magneto-mechanical bending moment compared to M2 and M4. Below 100 μT, however, the bending moment of M6 is not sufficient to overcome the high flexural rigidity of the overall device structure, leading to lower magneto-mechanical vibration amplitude. Furthermore, the generated peak voltage from the MME generators exhibited the same trend as the acceleration results (Fig. 2a and S5). M6 was found to generate the highest peak voltage of 44.8 V at 300 μT, while M4 generated the highest peak voltage of 20 V at 100 μT. The voltage amplitude and waveform generated from the generators were stable over ten days under 300 μT without significant degradation (Fig. S6).

To verify the experimental results and study the relationship between magneto-mechanical stress and generated piezoelectric potential in MME generators, we performed numerical modelling using finite element method (FEM). Details of the modelling method, boundary conditions, and results are provided in supporting information (Fig. S7-12 and Table S1-S3). The acceleration measured at tip mass of various MME generators was included in the model (Fig. 2b(i)), and internal stresses and corresponding piezoelectric potentials were calculated. Figure 2b(ii) shows the internal stress profile in the M4 generator under the magnetic field of 100 μT. Because of bending deformation, the first piezoelectric layer (Piezo1) and second piezoelectric layer (Piezo2) exhibited the opposite stress profiles with compressive stress and tensile stress, respectively. The neutral axis, which has zero stress during bending motion, is found to be located just above Piezo2 layer. The stress values at center of each piezo layer in the MME generator models were acquired under various external AC magnetic fields as shown in Fig. 2b(iii). This indicates that the stress amplitude in Piezo1 is much higher than that of Piezo2. In particular, the induced stress in Piezo1 layer of the M6 generator is slightly higher compared to M4 generator below 100 μT, in spite of the lower acceleration amplitude. This is because induced stress under the bending motion is generally proportional to the distance from the neutral axis and the bending moment following relation;[37]

$$\sigma = \frac{My}{I} \quad (4)$$

where σ, *y*, and *I* represent normal stress, distance from the neutral axis, and the moment of inertia, respectively. Resulting from the thicker magnetostrictive layers in the M6 generator, the Piezo1 layer is positioned relatively far away from the neutral axis compared with other generators as shown in Fig. S2. In contrast, Piezo2 layers in generators are located at same distance with respect to the neutral axis, which generates the same stress amplitude under same deflection. This is in agreement with the modeling results shown in Fig. 2(iii). Therefore, it can be concluded that the induced stress in Piezo1 layer mainly depends on the distance from the neutral axis, and the stress amplitude in Piezo2 layer is determined by the tip acceleration. Because of the high acceleration amplitude in M4 generator below 100 μT, the total stress on the piezoelectric layers in M4 generator is higher than other cases under low magnetic fields, resulting in higher voltage generation. The voltage output calculated from the stress amplitudes through the modeling exhibits similar

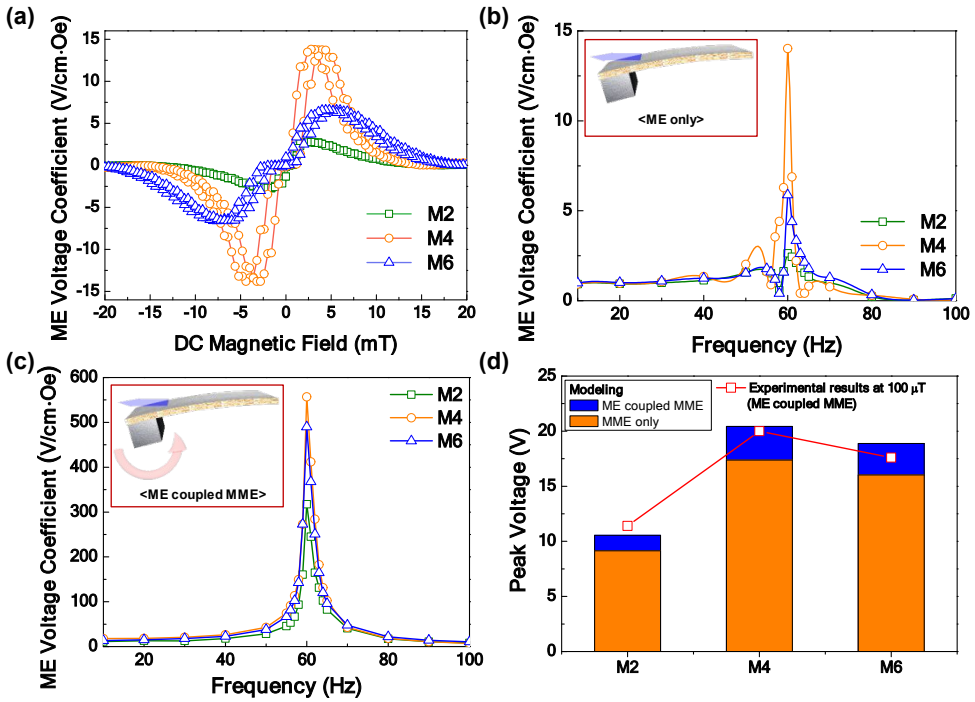

Fig. 3 Contribution of ME coupling on voltage output of the MME generators. (a) DC magnetic field dependent ME voltage coefficient of the MME generators with non-magnetic tip mass. (b) Frequency-dependent ME voltage coefficient of the MME generators with non-magnetic tip mass. (c) Frequency-dependent ME voltage coefficient of the MME generators with magnetic tip mass. (d) Calculated peak voltage output of the MME generators under 100 μT from the modelling. The blue bar indicates the peak voltage with the contribution of both ME coupling and magnetic torque, whereas orange bar is considered with only magnetic torque from the magnet tip.

trend to that of the experimental results (Fig. 2a). Through this structural analysis, we determined an optimum flexural rigidity and geometry of the MME harvester (M4), which maximizes voltage generation under the low magnetic fields.

Contribution of ME coupling on performance of MME generators

The amplitude of the ME coupling that is produced by the strain from the magnetostrictive layer is an important factor in determining the performance of the MME generator, as it also contributes towards total bending moment.[21] To understand the contribution of the ME coupling on the MME energy conversion, performance of the MME generators with and without contribution of magnetic torque from the magnetic tip mass was investigated through experimental and theoretical approach. The permanent magnetic tip mass was replaced by a non-magnetic tungsten mass with same weight to evaluate pristine ME coupling effect in each MME generator. Fig. 3a shows the ME coupling characteristics of the MME generators with the non-magnetic tip mass under 100 μT AC magnetic field at 60 Hz. The ME voltage coefficient is found to be maximized when a specific DC magnetic field is applied together with AC magnetic field. The frequency-dependent ME voltage coefficient indicates that the resonance frequency of MME generators is 60 Hz due to the same weight of the tip mass. The ME voltage coefficient of all the generators is maximized at the resonance frequency (Fig. 3b). Interestingly, M4 generator exhibited the highest ME voltage coefficient (~14 V/cm·Oe), although M6 generator includes a larger volume of the magnetostrictive layers, which mainly drives the magnetic bending moment. This indicates that the flexural rigidity of the generator also influences amplitude of the ME coupling and the bending moment produced from the magnetostrictive layers in the M6 generator may be insufficient to overcome its high flexural rigidity. With the magnetic tip mass, the MME generators exhibit ~4000% enhancement in ME voltage coefficient (557 V/cm·Oe in M4) as shown in Fig. 3b. This indicates that the bending moment is mostly produced by the magnetic torque from the magnetic tip mass and only small bending moment from the ME coupling contributes to the net MME energy conversion.

To verify the contribution of the ME coupling on the total bending moment and piezoelectric voltage generation, numerical modelling has been performed under similar conditions. The bending moment in the MME generator is derived for the composite beam consisting of piezoelectric and magnetostrictive layers.[38] The bending moment is then substituted in the force balance equations to obtain the governing equations of motion for the cantilever beam.[39] The piezoelectric coupling coefficient, G, is derived from the bending moment, shape function φ for the beam, and force balance in the case of asymmetric beam. The coupling coefficient, G, for the MME generators in this study can be obtained from the following expression,

$$\boldsymbol{G} = \frac{e_{31}\, b}{2}\left(\sum_{i=k}^{2k-2} \boldsymbol{t}_i + \frac{t_{k-1}+t_{2k-1}}{2}\right)\boldsymbol{\varphi}'|_L \qquad (5)$$

where, b, e_{31}, t_i, and L are beam width, equivalent piezoelectric stress coupling constant, thickness of layer, and tip of the beam, respectively. The k has the values of 4, 6 and 8 for M2, M4 and M6 generators, respectively. The force of excitation due to magnetostriction, F_{ms}, is given as

$$\boldsymbol{F_{ms}} = \sum_{i=1}^{n} \boldsymbol{e_{31mi} b\, t_i}\left(\sum_{k=1}^{i-1} \boldsymbol{t_k} + \frac{t_i}{2} - \bar{\boldsymbol{z}}\right)\boldsymbol{\varphi}'|_L \boldsymbol{H_1} \qquad (6)$$

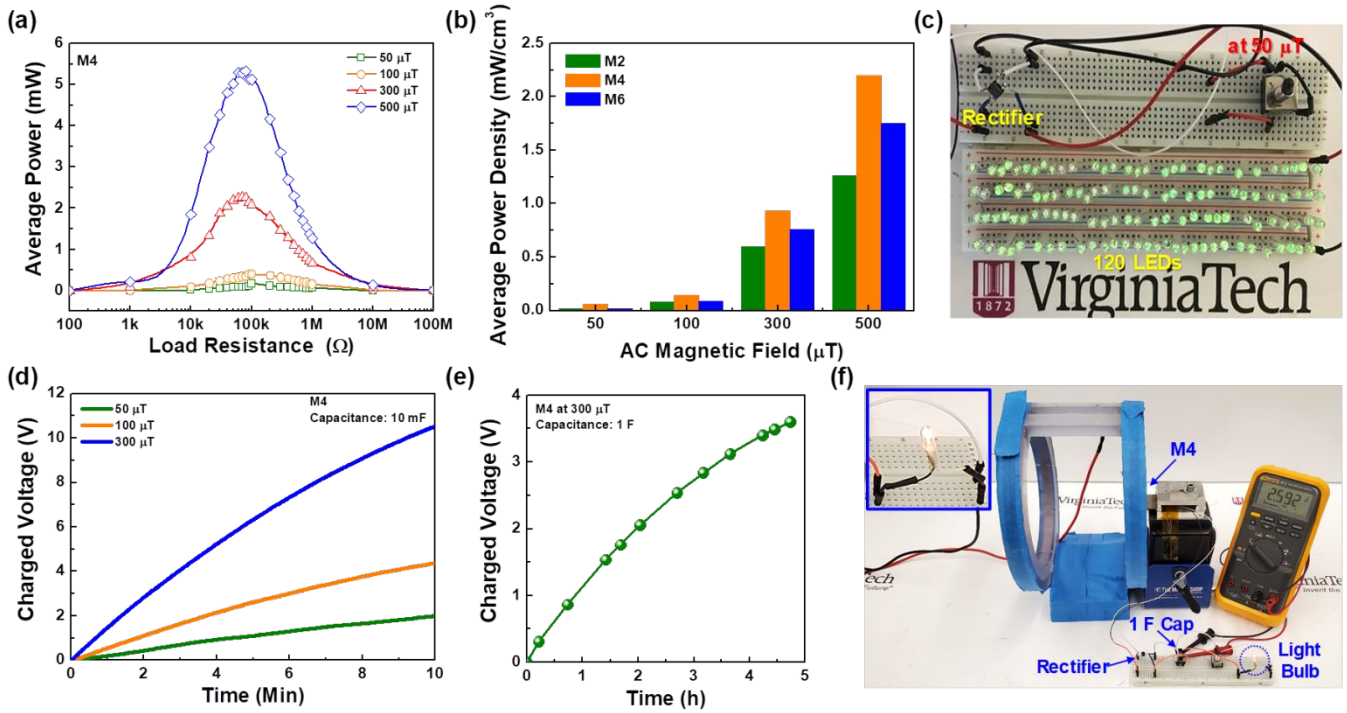

Fig. 4 Power output performance of MME generators. (a) Average power output of M4 generator under various magnetic field strength. (b) average power density of the MME generators under various magnetic field strength. (c) LEDs powered by M4 generator under 50 μT. (d) Charging curves for a 10 mF electrolytic capacitor under various magnetic field strength. (e) Charging curve for a 1 F supercapacitor under 300 μT. (f) Photograph of an incandescent light bulb turned on using the stored power in the 1 F supercapacitor. Inset shows a photo of lighted incandescent bulb.

where, e_{31mi} is the magnetostrictive stress constant of the i^{th} layer, which is obtained from magnetostriction curve of the pristine amorphous FBS alloy (Fig. S1), H_1 is the external magnetic field strength, and $\bar{z}$ is the height of the neutral axis. The total number of layers including the passive adhesive and piezoelectric layers is denoted by n. The force of excitation from a magnet is caused by the torque of the magnet in the oscillating magnetic field. Therefore, the force due to the magnetic tip mass (F_{mag}) can be obtained from the surface current model of the permanent magnet as

$$\boldsymbol{F_{mag} = wAB_r\varphi'(l)H_1(t)} \quad (7)$$

where, w, A, and B_r are width, projected area, and remnant flux density from the torque generated by the magnet, respectively. The MME generators were designed to resonate at 60 Hz by a magnetic and non-magnetic tip mass. The piezoelectric voltage is determined under applied forces both with ME coupled MME energy conversion (F_{ms} + F_{mag}) and only with MME energy conversion (F_{mag}). Details of modelling method and results are provided in supporting information S3 (Fig. S13 and S14, Table S4). Fig. 3c shows the peak voltage output of the MME generators under 100 μT from the modelling. The estimated peak voltage output of the ME coupled MME generator is similar to that of the experimental results (line plot). The ME coupling is found to enhance output voltage of the MME generator, in spite of much lower ME voltage coefficient produced without the magnetic tip. The output voltage is ~17.6% enhanced in the case of M4 generator with ME coupling, which results in ~38% enhancement in power output. From these results, we can conclude that the ME coupling plays a crucial role in amplification of the magneto-mechanical vibration amplitude, and enhancement of the voltage and power output performance for the MME generator.

Power generation

Power output of the MME generators was acquired by measuring the root-mean-square voltage (V_{RMS}) with various external load resistances (R_L) from 100 Ω to 100 MΩ. The average power (P_{avg}) was calculated through the following equation,

$$\boldsymbol{P_{avg} = \frac{V_{rms}^2}{R_L}} \quad (8)$$

Fig. 4a shows P_{avg} generated from M4 generator under various AC magnetic field strength. The P_{avg} is found to be maximized around 70 kΩ, which is aligned to the impedance value of the M4 generator at 60 Hz (Fig. S15). The M4 generator produces the maximum power of 0.17 and 0.4 mW_{avg} under 50 and 100 μT magnetic fields, respectively. Under the high magnetic field of 300 and 500 μT, the M4 generates milliwatt level power of 2.26 mW_{avg} and 5.32 mW_{avg}, respectively. Note that operation of the MME generators at more than 500 μT resulted in permanent device failure because the induced stress on the piezoelectric layers exceeds its tensile strength. As expected, the M6 generator produces slightly higher power under the high magnetic fields (2.7 mW_{avg} and 6.3 mW_{avg} at 300 and 500 μT, respectively) but M4 generator shows outstanding performance in the low magnetic field range (≤100 μT) (Fig. S16). Moreover, comparing the MME generators in power density, M4 exhibited the highest power output in overall magnetic field test range (Fig. 4b). The power density was calculated using the average power divided by volume of the MME generators including magnetic tip mass. The calculated power densities of the M4 generator were 0.06

mW_{avg}/cm^3, 0.15 mW_{avg}/cm^3, 0.94 mW_{avg}/cm^3, and 2.2 mW_{avg}/cm^3 under 50, 100, 300, and 500 μT, respectively. The M4 generator demonstrates a significant enhancement in power output compared to the previously reported MME generators that comprise of multi-layer Metglas laminates and piezoelectric MFC (~0.038 mW_{avg}/cm^3 under 100 μT and ~0.66 mW_{avg}/cm^3 under 500 μT).[21] The output power of M4 is found to be ~400% and ~330% higher than the previous MME generator under 100 μT and 500 μT, respectively. Further, the power output value exceeds that of previously reported MME generators in entire range of the magnetic field, such as Nickel/PMN-PZT SMFC generator: 0.046 mW/cm^3 at 160 μT,[22] PZT-5H/Brass composite generator: 11.73 $\mu W/cm^3$ at 100 μT, and Ni/Low-loss PMN-PZT SMFC generator: 2.1 mW_{DC}/cm^3 at 700 μT.[20] In particular, the power output performance under the high magnetic fields (≥500 μT), which is achieved through a structural design in this study utilizing commercially available materials, is comparable with the state-of-the-art MME harvesters that comprise of engineered materials, low-loss PMN-PZT SMFC and textured Fe-Ga alloy (4.6 mW_{avg} (3.22 mW_{DC}/cm^3) at 700 μT).[23]

To quantify the power output performance, we demonstrate powering arrays of light emitting diodes (LEDs) using the generated power from M4 harvester. To turn on the LEDs, a full bridge rectifier is connected as an AC-DC converter between M4 generator and LED arrays (Fig. S17a-c). Under 50 μT, M4 generator produces enough power to turn on 120 LEDs continuously without charging a capacitor (Fig. 4c). At a higher magnetic field of 300 μT, the M4 generator can turn on over 640 LEDs (Fig. S17d and Movie S1), which is significant performance compared to the LED powering results from previous studies.[20, 21, 23] Note that the previous studies powered the LEDs using far stronger magnetic fields. In another demonstration, we charged various capacitors to store generated electrical energy from M4 generator (Fig S18). A 10 mF electrolytic capacitor was charged under various magnetic field strength as shown in Fig. 4d. M4 generator charged the capacitor up to 2.6, 4.6, and 10.8 V within 10 minutes under the magnetic fields of 50, 100, and 300 μT, respectively. Under the 300 μT magnetic field, M4 generator was able to charge a 1 F supercapacitor up to 3.6 V (6.48 J) in only 4.7 hours, as shown in Fig. 4e. Note that charging a 1 F supercapacitor is a challenge in energy harvesting because of the high internal leakage current in the electrochemical supercapacitor. Using the stored energy, we demonstrated powering a small incandescent light bulb for over two minutes, which is the first attempt in piezoelectric based energy harvesting technologies (Fig. 4f and Movie S2).

Energy harvesting from ambient stray magnetic fields for operating wireless sensor communication system

The ultimate goal of this work was to harvest energy from ambient stray magnetic fields within infrastructure to provide a sustainable power source for operating IoT based wireless sensor communication systems. The stray magnetic fields exist everywhere in the modern infrastructures, but its amplitude is low in free space. Higher stray magnetic fields exist around home appliances, light elements, electronics, power transmission lines, etc. In particular, the electric devices generating high joule heating, such as heaters, electric irons, hair dryers, refrigerators, air conditioners, and lightings, radiate high amplitude of the stray magnetic field (see Table S5). To demonstrate the feasible operation of the ME coupled MME generator in real world condition, we utilized a space heater that generates relatively higher amplitude of the stray magnetic field.

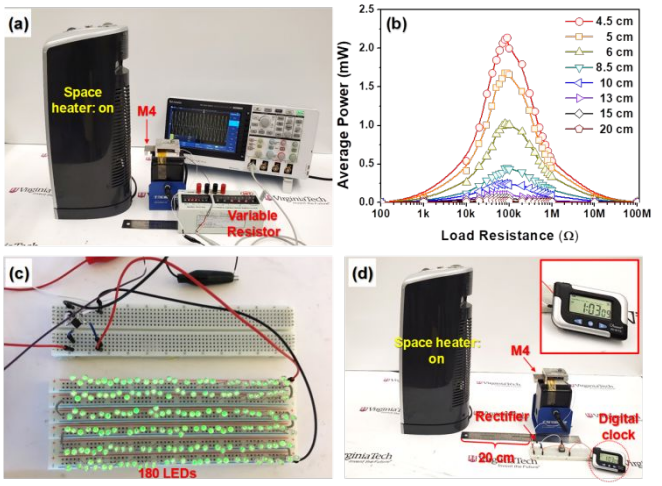

Fig. 5 Energy harvesting from ambient stray magnetic fields around space heater. (a) Experimental setup (b) Average power output with various distances between the generator and the space heater (c) The generated power at the distance of 10 cm is sufficient to continuously turn on 180 LED arrays. (d) The generated power at distance of 20 cm is sufficient to continuously power a digital clock without charging a capacitor or battery. The inset shows a photo of the digital clock operated by the generated power.

The M4 generator was placed at various distances (4.5 ~ 20 cm) away from the space heater for energy harvesting (Fig. 5a). Approximately 300, 200, 100, and 50 μT of magnetic fields were recorded at the distance of 4.5, 6, 8.5, and 13 cm, respectively. The power output from M4 generator at each distance is shown in Fig. 5(b). The M4 generator produced 2.13 mW_{avg} output power at 4.5 cm distance, which is similar to its output power under homogeneous magnetic field produced by Helmholtz coil (2.26 mW_{avg} at 300 μT). This indicates that our MME generator can meet the requirements in real condition without significant performance drop. The power output decreases upon increasing the distance between the space heater and MME generator. Placing the MME generator at 10 cm away from the space heater, which radiates a weaker magnetic field below 100 μT, the generated power is sufficient to power 180 LEDs brightly and continuously without charging a capacitor as shown in Fig. 5(c) and Movie S3. Even at a farther distance of 20 cm, where the magnetic field is weaker than 50 μT, the MME generator supplies sufficient power to operate a digital clock continuously without charging a capacitor (Fig. 5(d) and Movie S4).

To demonstrate wireless sensor communication systems powered by the MME generator, we used an integrated sensor including temperature, humidity, and acceleration sensors with a Bluetooth-based wireless data transmission system, which is a commercially available IoT component providing an efficient way to manage smart plants and smart offices through sensor communication and cloud computing systems. The sensor was placed in front of the space heater to detect the ambient temperature and humidity change during the operation of the space

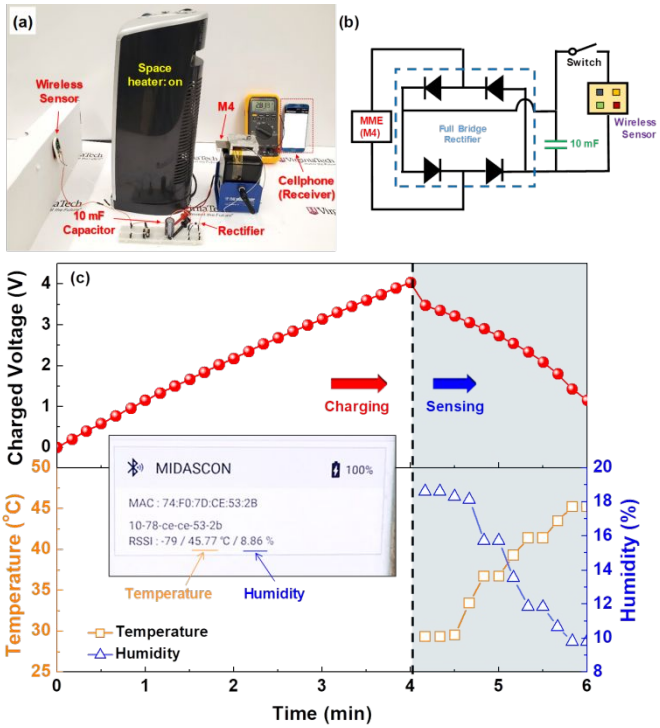

Fig. 6 Powering integrated sensor and wireless data transmission system. (a) Experimental setup. The wireless sensor is located in front of the space heater to detect ambient temperature and humidity change during the operation. (b) Electric circuit for the wireless sensor operation. (c) Charging and discharging curve of the 10 mF storage capacitor and transmitted data profile during the sensor operation.

heater (Fig. 6a). The M4 generator was placed at 4.5 cm distance from the space heater and connected to the sensor through a rectifier, 10 mF capacitor, and switch (Fig. 6b). A smartphone was used as a data receiver to acquire sensed information via Bluetooth. First, the M4 generator charges a 10 mF capacitor up to 4 V with switch-off status. When switch is on, the charged capacitor starts operating the sensor, and the data corresponding to temperature, humidity, and acceleration is sent to the smartphone simultaneously (Movie S5). Fig. 6c shows charging and discharging curves of the capacitor, and the data profile transmitted from the sensor during the cycle. The capacitor is charged up to 4 V in 240 s and the stored power operates the sensor for 120 s, while the voltage of the capacitor drops to 1.15 V. The capacitor can be recharged again up to 4 V within 2 min after the first cycle. The sensors transmitted the information on the temperature and humidity to the smartphone 12 times for 2 min. The profile of the ambient status around the sensor shows that the temperature increases and the humidity decreases, which is due to the hot and dry air from the heater. Table 1 shows a summary of recent progress of energy harvesting technologies that powered wireless sensors. [21-23, 40-44] The MME generator developed in this study produces higher power output, which can charge higher energy storage capacitors in shorter time periods, compared to other energy harvesting devices such as piezoelectric, triboelectric, and thermoelectric generators. Furthermore, among the state-of-art MME generators, M4 generator produces higher output energy under lower magnetic fields, that can operate multiple sensors and the Bluetooth data communication system simultaneously.

3. Conclusions

We demonstrate high power energy harvesting from low magnitude stray magnetic fields (≤300 μT) through the ME coupled MME energy conversion mechanism. Structural components in the ME coupled MME generator were designed to maximize the magneto-mechanical bending moment and stress applied on to the piezoelectric layer. The flexural rigidity of the generator, volume of the magnetic mass, and ME coupling coefficient are interrelated in controlling the energy conversion efficiency of the ME coupled MME generator. The bending moment from the magnetic torque and magnetostriction is maximized under a specific condition by modulating these three components. The maximum output power of 0.4 mW_{avg} was obtained from 100 μT magnetic field, which is >400% enhancement compared to the previously reported MME generators. The ME coupled MME generator was fabricated using commercially available materials. However, the MME generator still produced 5.32 mW_{avg} power under 500 μT magnetic field, which is comparable with the state-of-art MME generator that consist of single crystalline piezoelectric materials and textured magnetostrictive alloys.

Table 1. Recent progress on powering wireless sensors by various energy harvesting mechanisms.

Energy Harvesting Mechanism	Sensor	Capacitor Charging	Sensor Operation Time	Data Transmission	Ref #
Piezoelectric	Temperature	2 mF, 2.25 V for 50.5 s	Continuous with 1 min interval	RF	44
	Strain gauges	2 mF, 3.25 V for 8.3 s	Continuous with 8.3 s interval	Bluetooth	40
Thermoelectric	Temperature	2.2 mF for 5 min	~10 min with 30 s interval	Bluetooth	41
		100 mF, 3.3 V for 4 h			
Triboelectric	Pedometer	1 mF, for 21 s	Continuous with 21 s interval	Bluetooth	42
	Temperature	1 mF, ~3.2 V for ~1 h	~12 min with 35 s interval	RF	43
MME	Temperature	220 μF at 700 μT	Continuous with 5-10 s interval	RF	22
	Smart watch	2.2 mF + 1 mF, 3.6 V for 25 s at 700 μT	Continuous with ~5 s interval	RF	23
	Temperature, Humidity, and Acceleration	10 mF, 4 V for 5 min at 500 μT	~2 min with 10 s interval	Bluetooth	21
	Temperature, Humidity, and Acceleration	10 mF, 4 V for 4 min at **300 μT**	~2 min with 10 s interval	Bluetooth	**Present work**

Using the designed generator, we demonstrated energy harvesting around home appliances. The generated power was sufficient to operate integrated sensor and wireless data transmission systems. Structural innovation based on the fundamental understanding of the MME energy conversion resulted in the superior performance. The results provide a future direction for the magnetic field energy harvesting and integration with the IoT devices.

4. Methods

Fabrication of MME generators

To construct the MME generators, two piezoelectric plates (PSI-5A4E, Piezo System, Inc.) having silver electrode on both sides are laminated with magnetostrictive layers (2605SA, Metglas) using epoxy (DP-460, 3M) to form layered composite. To generate high voltage output, the piezoelectric plates are electrically connected in series with opposite poling directions. To ensure the series connection between the piezoelectric plates, piezoelectric and magnetostrictive layers are electrically connected by using a small amount of silver paste (Leitsilber 200 Silver Paint, Ted Pella) in the composite structure. To acquire power output from the device, electric wires are connected on both sides of the device using silver paste. Details on device fabrication procedure and configuration are provided in Fig S19 in supplementary information section 6.

Characterization

A Helmholtz coil controlled by a lock-in amplifier (SR830, Stanford Research Systems) was used as an AC magnetic field source. The MME generators were placed at the center of the circular structure of the coil to apply homogeneous magnetic fields to the MME generators. To apply accurate amplitudes of AC magnetic fields, the AC magnetic field was calculated based on the number of turns of the coil, and it was confirmed through measuring the AC magnetic fields using a gauss meter. The open-circuit voltage was measured using an oscilloscope (Keysight DSO1014A) under various magnetic field strength. To calculate the average power, the RMS voltage was measured with variable resistor from 100 Ω to open-circuit. The power density was calculated with average power divided by the entire volume of the generators including the tip mass. The acceleration of the tip vibration was measured using a scanning vibrometer (Polytec PSV-500). To measure the ME voltage coefficients of the MME generators with non-magnet tip mass, an electromagnet (GMW Magnet System, Model: 3472-70) was employed to supply DC magnetic fields, while the Helmholtz coil supplies a fixed AC magnetic field of 100 μT at 60 Hz. The clamped MME generators were placed laterally in the middle of the Helmholtz coil where the DC and AC magnetic fields are aligned. The RMS AC voltage produced from the MME generator measured in a range of -20 and 20 mT DC magnetic field using a lock-in amplifier. The ME voltage coefficient was calculated using an equation of $V_{RMS}/t_{PZT}{\cdot}H_{AC}$, where V_{RMS}, t_{Piezo}, and H_{AC} are RMS voltage, thickness of the piezoelectric layers, and external AC magnetic field, respectively. The ME voltage of the MME generators with the magnetic tip mass was measured under 100 μT AC magnetic field at 60 Hz without DC magnetic field. To quantify the generated power, commercial green LEDs were powered and various capacitors were charged using the generated power from the MME generators. A bridge rectifier (MB1S-TP, Micro Commercial Co.), which enables AC-DC converting, was used for the LED lighting and capacitor charging.

Modelling

To investigate relationship between flexural rigidity and voltage output, stress, strain, and piezoelectric potential profiles in the MME generators have been modeled by using COMSOL Multi-physics with the piezoelectric module. The modelling to study the contribution of the ME coupling on the output voltage of the MME generator has been performed using Wolfram Mathematica software with four levels of magnetic field flux density conditions (50, 100, 300 and 500 μT). Details of the modeling methods and conditions are provided in Supporting Information.

Power generation from ambient stray magnetic field and powering wireless sensors

To demonstrate power generation in real world, the MME generator was placed under ambient stray magnetic fields around a space heater (120 V, 60 Hz, 1500 W, Intertek, Model: 5367). The average power output was obtained at various distances from the space heater. To quantify the output performance of the MME generator, LED arrays and a digital clock were powered using output power from the MME generator. The integrated wireless sensor communication system (MIDASCON, Hanvit SI., Inc.) was used to demonstrate powering IoT component by the MME generator. A smartphone (Galaxy S7 Edge, Samsung Electronics) was used as a data receiver.

Conflicts of interest

There are no conflicts to declare.

Acknowledgements

H.L. and M.G.K. acknowledge the financial support from Office of Naval Research through grant N000141613043. S.P. acknowledges support from National Science Foundation (NSF) through EAGER program (1832865) and R.S.R acknowledges support from NSF-CREST through grant number HRD 1547771. P.K. acknowledges support from Office of Naval Research through grant number N000141712520.

References

1. N. Gershenfeld, S. Samouhos and B. Nordman, *Science*, 2010, **327**, 1086-1088.
2. R. Haight, W. Haensch and D. Friedman, *Science*, 2016, **353**, 124-125.
3. J. M. Perkel, *Nature*, 2017, **542**, 125-126.
4. N. Wang, *Nat. Energy*, 2018, **3**, 907-909.

5. C. Jiang, H. W. Choi, X. Cheng, H. B. Ma, D. Hasko and A. Nathan, *Science*, 2019, **363**, 719-723.
6. C. Lethien, J. Le Bideau and T. Brousse, *Energy Environ. Sci.*, 2019, **12**, 96-115.
7. C. Bowen, H. Kim, P. Weaver and S. Dunn, *Energy Environ. Sci.*, 2014, **7**, 25-44.
8. Z. L. Wang, J. Chen and L. Lin, *Energy Environ. Sci.*, 2015, **8**, 2250-2282.
9. G. Z. Zhang, P. Zhao, X. S. Zhang, K. Han, T. K. Zhao, Y. Zhang, C. K. Jeong, S. L. Jiang, S. L. Zhang and Q. Wang, *Energy Environ. Sci.*, 2018, **11**.
10. X. Wang, S. H. Wang, Y. Yang and Z. L. Wang, *ACS Nano*, 2015, **9**, 4553-4562.
11. K. W. Zhang, X. Wang, Y. Yang and Z. L. Wang, *ACS Nano*, 2015, **9**, 3521-3529.
12. K. W. Zhang, Y. O. H. Wang and Y. Yang, *Adv. Funct. Mater.*, 2019, **29**.
13. G. Vats, A. Kumar, N. Ortega, C. R. Bowen and R. S. Katiyar, *Energy Environ. Sci.*, 2016, **9**, 1335-1345.
14. F. Kim, B. Kwon, Y. Eom, J. E. Lee, S. Park, S. Jo, S. H. Park, B. S. Kim, H. J. Im, M. H. Lee, T. S. Min, K. T. Kim, H. G. Chae, W. P. King and J. S. Son, *Nat. Energy*, 2018, **3**, 301-309.
15. L. Donaldson, *Mater. Today*, 2018, **21**.
16. S. Yun, Y. Qin, A. R. Uhl, N. Vlachopoulos, M. Yin, D. D. Li, X. Han and A. Hagfeldt, *Energy Environ. Sci.*, 2018.
17. A. Pieper, M. Hohgardt, M. Willich, D. A. Gacek, N. Hafi, D. Pfennig, A. Albrecht and P. J. Walla, *Nat. Comm.*, 2018, **9**, 666.
18. L. Winkless, *Mater. Today*, 2018, **21**, 691-691.
19. S. H. Kim, C. S. Haines, N. Li, K. J. Kim, T. J. Mun, C. Choi, J. T. Di, Y. J. Oh, J. P. Oviedo, J. Bykova, S. L. Fang, N. Jiang, Z. F. Liu, R. Wang, P. Kumar, R. Qiao, S. Priya, K. Cho, M. Kim, M. S. Lucas, L. F. Drummy, B. Maruyama, D. Y. Lee, X. Lepro, E. L. Gao, D. Albarq, R. Ovalle-Robles, S. J. Kim and R. H. Baughman, *Science*, 2017, **357**, 773-778.
20. V. Annapureddy, M. Kim, H. Palneedi, H. Y. Lee, S. Y. Choi, W. H. Yoon, D. S. Park, J. J. Choi, B. D. Hahn and C. W. Ahn, *Adv. Energy Mater.*, 2016, **6**.
21. M. G. Kang, R. Sriramdas, H. Lee, J. Chun, D. Maurya, G. T. Hwang, J. Ryu and S. Priya, *Adv. Energy Mater.*, 2018, **8**, 1703313.
22. J. Ryu, J.-E. Kang, Y. Zhou, S.-Y. Choi, W.-H. Yoon, D.-S. Park, J.-J. Choi, B.-D. Hahn, C.-W. Ahn and J.-W. Kim, *Energy Environ. Sci.*, 2015, **8**, 2402-2408.
23. V. Annapureddy, S.-M. Na, G.-T. Hwang, M. G. Kang, R. Sriramdas, H. Palneedi, W.-H. Yoon, B.-D. Hahn, J.-W. Kim and C.-W. Ahn, *Energy Environ. Sci.*, 2018.
24. G. Liu, P. Ci and S. Dong, *J. Appl. Phys.*, 2014, **115**, 164104.
25. G. Liu, X. Li, J. Chen, H. Shi, W. Xiao and S. Dong, *Appl. Phys. Lett.*, 2012, **101**, 142904.
26. D. R. Patil, Y. Zhou, J.-E. Kang, N. Sharpes, D.-Y. Jeong, Y.-D. Kim, K. H. Kim, S. Priya and J. Ryu, *APL Mater.*, 2014, **2**, 046102.
27. Z. Xing, K. Xu, G. Dai, J. Li and D. Viehland, *J. Appl. Phys.*, 2011, **110**, 104510.
28. X. Z. Wei, Z. S. Wang and H. F. Dai, *Energies*, 2014, **7**, 4316-4341.
29. A. Kurs, A. Karalis, R. Moffatt, J. D. Joannopoulos, P. Fisher and M. Soljacic, *Science*, 2007, **317**, 83-86.
30. X. Zhang, J. Grajal, J. L. Vazquez-Roy, U. Radhakrishna, X. X. Wang, W. Chern, L. Zhou, Y. X. Lin, P. C. Shen, X. Ji, X. Ling, A. Zubair, Y. H. Zhang, H. Wang, M. Dubey, J. Kong, M. Dresselhaus and T. Palacios, *Nature*, 2019, **566**, 368-+.
31. A. Ahlbom, U. Bergqvist, J. Bernhardt, J. Cesarini, M. Grandolfo, M. Hietanen, A. Mckinlay, M. Repacholi, D. Sliney and J. A. Stolwijk, *Health Phys.*, 1998, **74**, 494-521.
32. Electromagnetic fields (EMF) https://www.who.int/peh-emf, (accessed April 9, 2019).
33. M. G. Kang, W. S. Jung, C. Y. Kang and S. J. Yoon, *Actuators*, 2016, **5**, 5.
34. S. Priya and D. J. Inman, *Energy harvesting technologies*, Springer, New York ; London, 2009.
35. Z. P. Xing, K. Xu, G. Y. Dai, J. F. Li and D. Viehland, *J Appl Phys*, 2011, **110**, 104510.
36. Y. Zhang, Q. Ren and Y. P. Zhao, *J. Phys. D Appl. Phys.*, 2004, **37**, 2140-2145.
37. R. C. Hibbeler, *Mechanics of materials*, Tenth edition. edn.
38. A. Erturk and D. J. Inman, *Piezoelectric energy harvesting*, Wiley, Chichester, 2011.
39. R. Sriramdas, S. Chiplunkar, R. M. Cuduvally and R. Pratap, *IEEE Sens. J.*, 2015, **15**, 3338-3348.
40. J. Lee and B. Choi, *Energ Convers Manage*, 2014, **78**, 32-38.
41. B. Iezzi, K. Ankireddy, J. Twiddy, M. D. Losego and J. S. Jur, *Appl. Energy*, 2017, **208**, 758-765.
42. L. Jin, J. Chen, B. B. Zhang, W. L. Deng, L. Zhang, H. T. Zhang, X. Huang, M. H. Zhu, W. Q. Yang and Z. L. Wang, *ACS Nano*, 2016, **10**, 7874-7881.
43. A. Ahmed, Z. Saadatnia, I. Hassan, Y. L. Zi, Y. Xi, X. He, J. Zu and Z. L. Wang, *Adv. Energy Mater.*, 2017, **7**.
44. Y. H. Han, Y. Feng, Z. J. Yu, W. Z. Lou and H. C. Liu, *IEEE Sens. J.*, 2017, **17**, 6770-6777.